

Discovery of a low-mass companion embedded in the disk of the young massive star MWC 297 with VLT/SPHERE*

M. GIULIA UBEIRA-GABELLINI^{1,2}

VALENTIN CHRISTIAENS³

GIUSEPPE LODATO¹

MARIO VAN DEN ANCKER²

DAVIDE FEDELE⁴

CARLO F. MANARA²

DANIEL J. PRICE³

¹*Dipartimento di Fisica, Università Degli Studi di Milano,
Via Celoria, 16, Milano, I-20133, Italy.*

²*European Southern Observatory,
Karl-Schwarzschild-Str. 2,
D-85748 Garching bei München, Germany.*

³*School of Physics and Astronomy,
Monash University, Clayton VIC 3800, Australia*

⁴*INAF - Osservatorio Astrofisico di Arcetri,
Largo E. Fermi 5, I-50125 Firenze, Italy.*

(Received December 2, 2019; Revised January 23, 2020; Accepted January 27, 2020)

Submitted to ApJL

ABSTRACT

We report the discovery of a low-mass stellar companion around the young Herbig Be star MWC 297. We performed multi-epoch high-contrast imaging in the near infrared (NIR) with the Very Large Telescope (VLT)/Spectro-Polarimetric High-contrast Exoplanet REsearch (SPHERE) instrument. The companion is found at projected separation of 244.7 ± 13.2 au and a position angle of 176.4 ± 0.1 deg. The large separation supports formation via gravitational instability. From the spectrum, we estimate a mass of $0.1\text{--}0.5\text{ M}_{\odot}$, the range conveying uncertainties in the extinction of the companion and in evolutionary models at young ages. The orbit coincides with a gap in the dust disk inferred from the Spectral Energy Distribution (SED). The young age ($\lesssim 1$ Myr) and mass ratio with the central star (~ 0.01) makes the companion comparable to PDS 70 b, suggesting a relation between formation scenarios and disk dynamics.

Keywords: methods: observational — instrumentation: adaptive optics — techniques: high angular resolution — stars: low-mass — stars: early-type

1. INTRODUCTION

Binary star formation theories such as disk fragmentation (Bonnell 1994), capture (Tohline 2002), or core fragmentation (Bonnell et al. 1991) are best tested with direct imaging of young objects. But the number of low-mass companions around pre-main-sequence stars

Corresponding author: Maria Giulia Ubeira Gabellini
maria.ubeira@unimi.it

* Based on observations performed with ESO Telescopes at Paranal Observatory under programs 095.C-0787 and 0101.C-0350.

detected by direct imaging remains low (e.g. [Bowler 2016](#)). The situation is improving thanks to purpose-built high-contrast instruments such as the Spectro-Polarimetric High-contrast Exoplanet REsearch instrument (SPHERE, [Beuzit et al. 2008](#)) at the Very Large Telescope (VLT) and Gemini Planet Imager (GPI, [Macintosh et al. 2014](#)). Using these new instruments, [Keppler et al. \(2018\)](#) detected and confirmed a companion within the gap of the transition disk around PDS 70.

In this Letter we report the discovery of a low-mass companion in the disk around Herbig Be star MWC 297 using high-contrast observations with VLT/SPHERE-IFS.

2. MWC 297

MWC 297 (RA(J2000) = 18 27 39.527, Dec(J2000) = -03 49 52.05) is a young pre-main-sequence ($< 1\text{Myr}$) Herbig Be star (spectral type B1.5), with $M_\star \sim 17 M_\odot$ ([Vioque et al. 2018](#)) located in the L515 region at a distance of ~ 375 pc ([Vioque et al. 2018](#), Gaia DR2). It was classified as a Class II, Group I source ([Meeus et al. 2001](#)) from SED fitting ([Mannings 1994](#)). From the mm-spectral slope of the SED, [Manoj et al. \(2007\)](#) argued for either a compact disk or for grain growth in the circumstellar environment. The system has a compact circumstellar disk ([Weigelt et al. 2011](#), Br γ and NIR continuum visibilities study) and with low inclination ($\sim 5^\circ$, [Alonso-Albi et al. 2009](#)). Finally, [Alonso-Albi et al. \(2009\)](#) observed the disk at millimeter wavelengths with the Very Large Array. They modeled the SED using a two-component disk, with inner (~ 7.5 to 43.5 au) and outer (~ 300 to 450 au) parts and a gap in between. Both the presence of a companion or grain growth in the outer disk may explain such a gap. The authors ruled out a companion due to the apparent non-detection of any point-like source at the suggested distance (~ 270 au when rescaled to Gaia distance).

3. OBSERVATIONS AND DATA REDUCTION

3.1. Derivation of stellar properties

Table 1 summarizes the stellar and disk properties. The effective temperature and interstellar extinction were derived following [van den Ancker et al. \(1998\)](#): the observed SED (between $0.3 - 1.2 \mu\text{m}$) was fitted using atmospheric models of [Kurucz \(1991\)](#) and the dereddening law from [Cardelli et al. \(1989\)](#) with $R_v=3.1$. The stellar radius was estimated based on L_{bol} and T_{eff} .

3.2. Observations

We observed MWC 297 on April 29, 2015 and on June 28, 2018 with SPHERE in the IRDIFS-EXT mode i.e.

Table 1. Physical properties of MWC 297

Param.	Units	Value	References
d	pc	375 ± 20	Gaia Collaboration et al. (2018)
Age	Myr	< 1	Acke & van den Ancker (2006)
			Vioque et al. (2018)
Sp.T.		B1.5Ve	Drew et al. (1997)
Group		I	Meeus et al. (2001)
T_{eff}	K	23700	this work
A_v	mag	7.72	this work
$\log(L_{\text{bol}})$	L_\odot	4.59	Vioque et al. (2018)
M_\star	M_\odot	16.9	Vioque et al. (2018)
R_\star	R_\odot	9.17	this work

Notes. d : Gaia distance; Sp.T.: spectral type; Group: Disk classification according to [Meeus et al. \(2001\)](#); T_{eff} : effective temperature, A_v : extinction, L_{bol} : bolometric luminosity; M_\star : stellar mass; and R_\star : stellar radius.

simultaneous Integral Field Spectroscopy (IFS) in the YJH bands, and dual-band imaging in the K band. The first observation (2015-04-29) was taken in field tracking mode, while for the second set (2018-07-28) we used the pupil tracking mode (Table 2). The IFS data are cubes of 39 monochromatic images in the NIR encompassing a Field of view of $1.''73 \times 1.''73$. The spectral resolution was $R \sim 30$ for the IRDIFS-EXT mode ($Y-H$, $0.95 < \lambda < 1.65 \mu\text{m}$). The N-ALC-YJH-S coronagraph (inner working angle $\sim 0.''15$) was used.

We obtained “Flux” and “Star Center” calibration images at the beginning and end of both observing sequences. The “Flux” images were obtained by offsetting the central star from the coronagraphic spot and used to measure the unsaturated peak flux of the star. The “Star Center” images allowed us to measure the position of the star behind the coronagraph, located at the center of the four replicas produced by the adaptive optics system.

3.3. Data reduction

We used the ESO pipeline¹ to reduce the IFS data. We used a function implemented in the Vortex Imaging Pipeline² (VIP, [Gomez Gonzalez et al. 2017](#)) to correct for clumps of bad pixels through an iterative sigma filtering process. For the centering, we increase the signal-to-noise (SNR) of the star replicas using a high-pass filter that subtracts the image itself with a median low-pass filtered version of the image. We fitted the four replicas with a 2D Moffat function (in VIP) to derive the cen-

¹ <http://www.eso.org/sci/software/pipelines/sphere/>; v0.24.0, for the first dataset; v0.36.0, for the recent data.

² <https://github.com/vortex-exoplanet/VIP>.

troid of the star in each frame. We then interpolated the values of the derived center (taken at the beginning and end of the observations) considering the observation time of the science images. Finally, the error was considered to be the discrepancy in the value between two sequential sets of center images (on average $\sigma_x=0.04$ pixels and $\sigma_y=0.08$ pixels).

3.4. Post-processing using VIP

Calibrated frames are still affected by quasi-static speckles produced by the star (Marois et al. 2006). Speckles move radially with wavelength, while real features remain fixed (spectral information). This is key to the Spectral Differential Imaging (SDI) algorithm (e.g., Sparks & Ford 2002). Also, fixing the pupil of an altitude-azimuth telescope during an observing sequence, most quasi-static speckles remain fixed in the image, while real features rotate (angular information). Angular Differential Imaging (ADI; e.g., Marois et al. 2006) is based on this idea. The IFS cubes contain the spectral information, while angular information is available when the rotator is moved to maintain the pupil fixed. We used principal component analysis (PCA)-based algorithms in VIP to model and subtract the stellar point-spread function (PSF) and associated speckles. For both sets of observations we applied PCA-SDI, using the spectral information alone, and PCA-SADI, where the PCA library was built using both the angular and spectral information (Pueyo et al. 2012). We also tested the algorithm in two separate steps (PCA-SDI + PCA-ADI; Christiaens et al. 2019), but obtained noisy final images. For the second observational set, we also used another algorithm: PCA-ADI, using only the angular information, performed either in full frames (Soummer et al. 2012) or in concentric 2-FWHM wide annuli on individual spectral channels (Absil et al. 2013).

4. CHARACTERIZATION OF THE COMPANION

4.1. 2015 detection

We detected a bright companion in the outer disk of MWC 297 on 29th April 2015 located ~ 246.4 au from the central star. The detection was obtained using the PCA-SADI (Fig. 1, top left) and PCA-SDI techniques, with 4σ and 5σ significance. The companion was detected in the averaged H -band image ($\text{SNR} \gtrsim 4$), but not in J and Y .

4.2. 2018 detection

We performed follow-up observations with longer integration time (Table 2) on 28th July 2018. We re-detected the companion in H and J -bands with four different post-processing methods ($\text{SNR} > 4$). We detected

it also in the Y -band just using ADI. Figure 1 shows that the point-like source is detected regardless of the post-processing method (SADI, ADI, ANNULI and SDI — not shown here) and of wavelength (H , J and Y bands all show the companion).

4.3. Spectro-astrometry

We used the Markov Chain Monte Carlo (MCMC), a nested sampling algorithm coupled to the negative fake companion technique implemented in VIP to derive the position and the flux of the companion at each wavelength (e.g. Marois et al. 2010; Wertz et al. 2017). We first estimated the position and flux using the Nelder-Mead simplex-based algorithm (Nelder & Mead 1965), and then fed these first estimates to the MCMC routine. A negative PSF was injected in the original data cube in order to completely delete the signal of the real companion measured in the final PCA-ADI post-processed image. The process produces a posterior distribution of the three parameters and stops upon convergence to minimal absolute residuals in an aperture centered on the location of the companion. Finally, this routine gave us the companion separation, position angle and flux, with errors (Table 2).

4.3.1. Astrometry

Using MCMC on the second epoch, we derived the position (r and PA) and relative error of the companion for each wavelength and computed the weighted average (Figure 2, panel a, b; red line). For the first epoch, it was not possible to use MCMC. We therefore fitted a 2D Gaussian to derive the position and took the weighted average of the results of the SDI and SADI methods. We considered a pixel scale of 7.46 ± 0.02 mas/pixel (Maire et al. 2016). The separation uncertainty was computed as a sum in quadrature of the uncertainties on the stellar and companion position and on the pixel scale for each frame (Figure 2, panel a; Table 2). We took into account the target distance error to derive the separation in au (Table 2).

The position angle (PA) is affected by the error on the True North angle determination of -102.18 ± 0.13 deg (Maire et al. 2016), used to derive the astrometry. We propagated the errors in the position and true north to get the final error (panel b, Figure 2, Table 2).

Figure 2 (panel d) suggests a companion comoving with the host star on a trajectory more consistent with Keplerian motion. A background star would move on the trajectory shown by the black line: its proper motion after 3.25 yr exceeds the centroid discrepancy of the two observation sets (orange and blue), albeit within 2σ uncertainty. Assuming a face-on circular orbit (recalling the $\sim 5^\circ$ disk inclination), Keplerian motion would

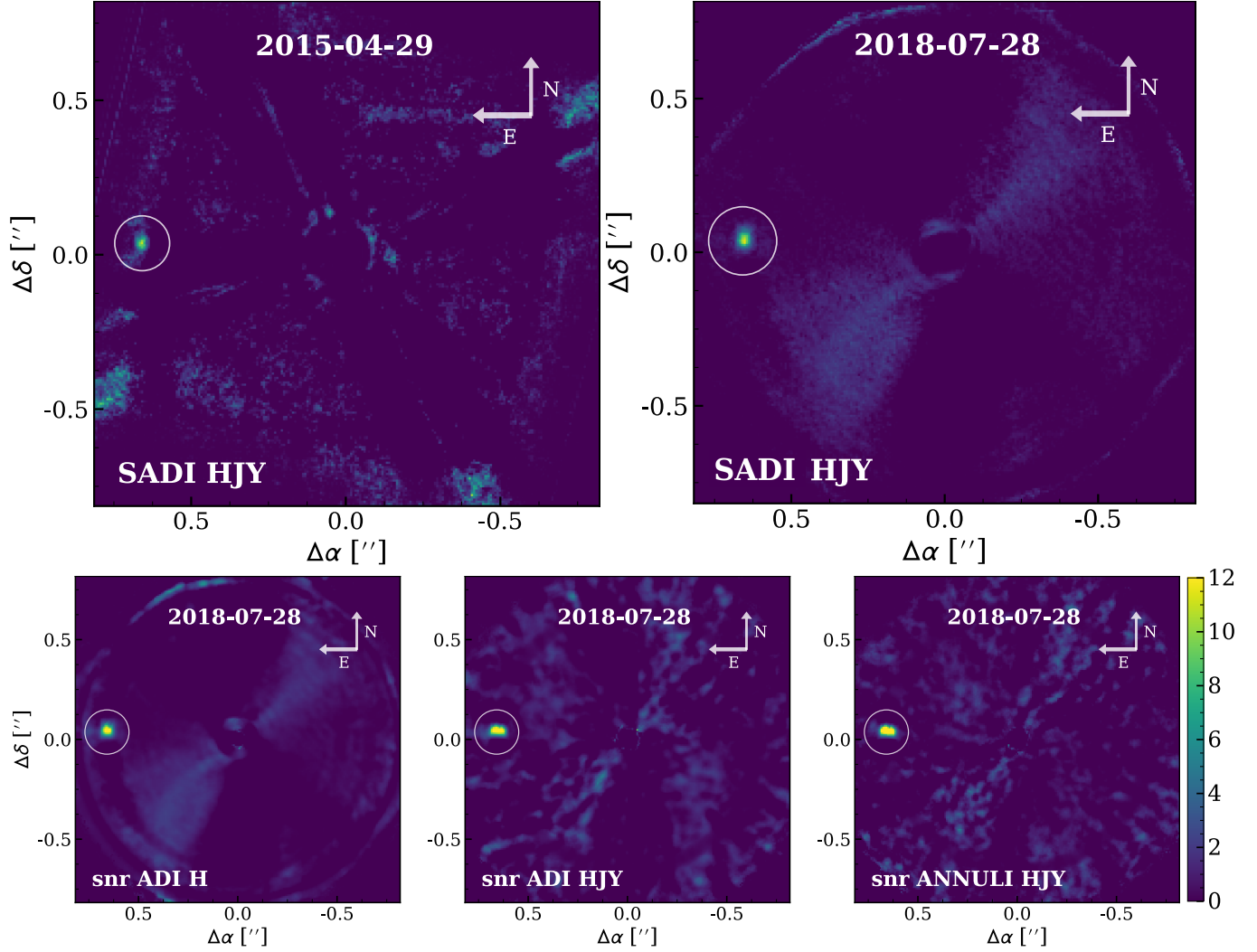


Figure 1. Top: MWC 297B detected with SADI in 2015 (left) and 2018 (right) combining all wavelengths. Bottom: SNR (day: 2018-07-28) using ADI performed in full frame with just H-Band frames (left), with all frames combined (center) and done in annuli (right). The companion is always detected (white circle), irrespective of technique. We also detected the companion in J and Y Band images with ADI, but fainter.

account for a shift in position angle of 1.26° , inside the error bar of the first detection.

Our two-epoch astrometry alone does not rule out the possibility of a background object. Therefore, we used the TRILEGAL model of the Galaxy to estimate the probability of being a background star (Girardi et al. 2005). TRILEGAL yields 6553 stars with an H -band apparent magnitude brighter or equal to that of our companion candidate ($H \leq 13.84$ mag; Sec. 4.3.2) within a $30' \times 30'$ patch of sky centered on the star, hence a density of $0.002 \text{ arcsec}^{-2}$. The probability is thus $1 - \mathcal{P}(n = 0 | \lambda = 0.002, B = 4) \approx 0.8\%$, where $\mathcal{P}(\lambda, B)$ is the spatial homogeneous Poisson point process probability with rate λ and area B . Given the separation of $\sim 0.7''$, we conservatively consider a $2'' \times 2''$ box centered on the star for the area.

4.3.2. Spectro-photometry

The longer integration time of the 2018 data allowed us to detect the companion candidate at a significant level in all Y, J and H bands (Fig. 1, center left, shows H band), and to derive its spectrum (Figure 2, panel c). For each spectral frame, we measured the flux from the star using the “Flux” image and the companion flux using the MCMC method described in Section 4.3. The stellar flux error was considered as the discrepancy between two sets of “Flux” images.

To produce the final calibrated spectrum (Figure 2, panel c), we multiplied the measured spectrum of the companion by the ratio between the stellar flux in physical units, obtained through a polynomial fit of the stellar SED in the IFS wavelength range, and in ADUs in each

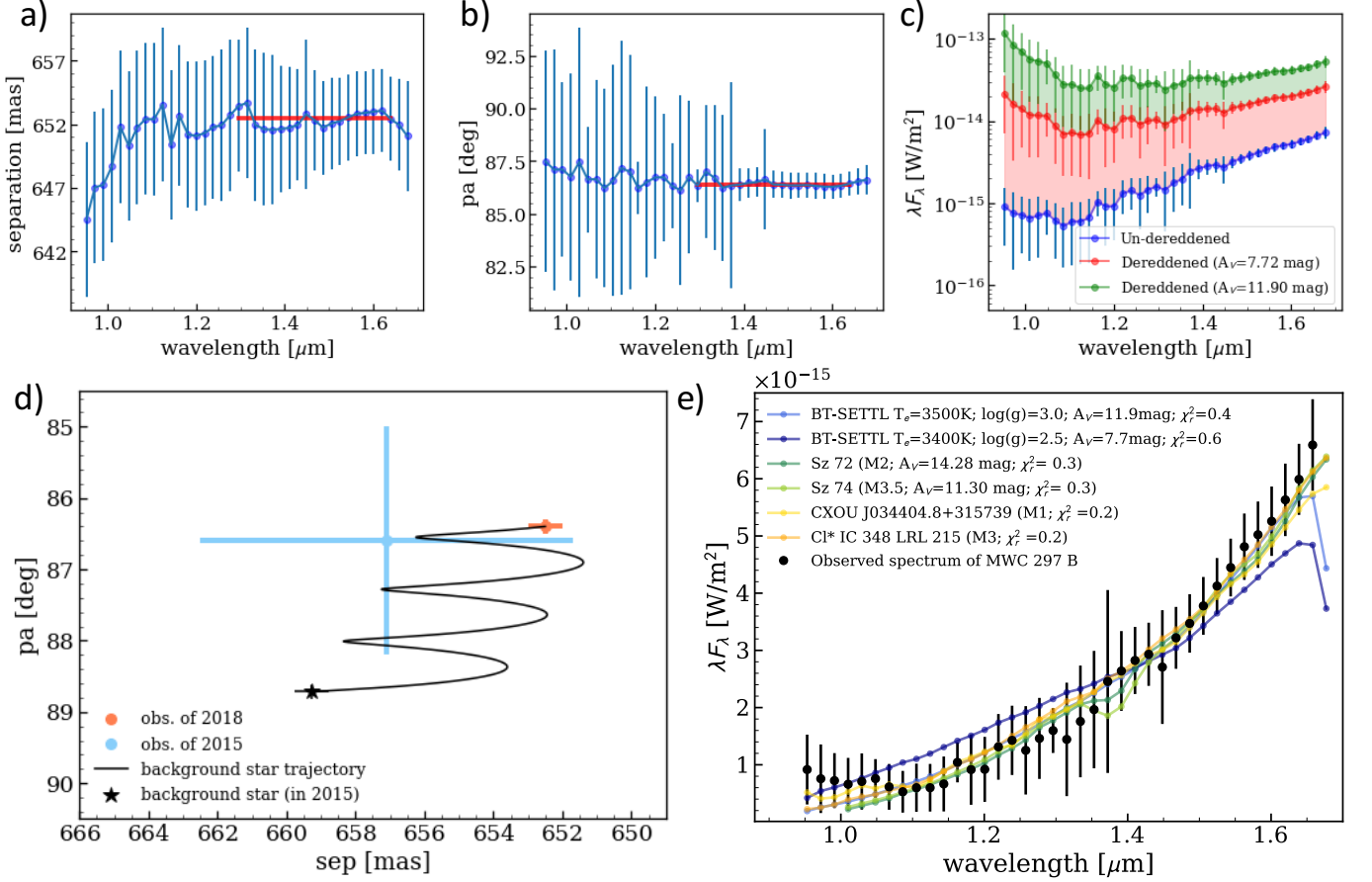


Figure 2. Top: MCMC fit (on second epoch) for separation (left) and position angle (center). Red lines show weighted average, inferred where the SNR is highest ($1.29\mu\text{m} \lesssim \lambda \lesssim 1.64\mu\text{m}$). Top right: IFS spectrum of companion in physical units, shown underreddened (*blue points*), dereddened with the stellar extinction (*red points*), and with $A_V=11.9$ mag (*green points*). Bottom left: Companion astrometry on the two datasets with their 1σ uncertainties (first epoch: light blue, second epoch: orange; Table 2). Black line shows the trajectory for a background star going back to the 2015 epoch. Bottom right: Best-fit BT-SETTL models with extinction as free parameter (light blue) and with A_V inferred from the central star (dark blue); best-fit YSOs (green) and SpeX template spectra (yellow).

spectral channel. For completeness, we also measured the total emission of the companion over the star in bands H , J and Y with errors (Table 2) and derived the apparent magnitude of the companion in those bands (13.86 mag, 16.21 mag and 17.30 mag, respectively).

4.4. Spectral analysis

The underreddened spectrum of the companion (Fig. 2, panel c; *blue points*) shows a very red slope, suggesting significant extinction on the companion, not necessarily the same of the star. Each component might be embedded and surrounded by their own disk, in addition to any remnant envelope (e.g. Bowler et al. 2014; Mesa et al. 2019). Therefore, following Christiaens et al. (2018), we considered extinction as a free parameter when fitting BT-SETTL models (Allard et al. 2012). Our grid of BT-SETTL models contains four free parameters: Ef-

fective temperature, $T_{\text{eff}} \in [1200\text{K}, 5500\text{K}]$ in 100K steps; surface gravity, $\log(g) \in [2.5, 5.0]$ in 0.5dex steps; radius, $R_B \in [0.1 R_\odot, 3.5 R_\odot]$ in 0.01 R_\odot steps; and extinction, $A_V \in [0, 21]$ mag in 0.1 mag steps. We then considered the same grid, but we fixed the extinction to $A_V=7.72$ mag (Figure 2, panel c, *red points*), same as for the central star (Section 2).

Next, we considered two libraries of young stellar objects (YSOs) template spectra: (i) all 76 pre-main sequence stars spectra compiled in Alcalá et al. (2014) and Manara et al. (2013, 2017), which are members of the TW Hya, σ Ori, Lupus I, III and IV star forming regions, spanning G5 to M8.5 spectral types; and (ii) all young dwarfs from the SpeX library (Burgasser 2014), identified based on their gravity class or their membership to young (< 10 Myr old) clusters. In either cases, we considered two free parameters to account for dif-

ferent A_V and distance between observed and template spectra.

For all spectral fits, we convolved the models and templates with the IFS spectral response before binning them to the same wavelength sampling. We then minimized a goodness-of-fit indicator χ^2 that accounts for the spectral covariance of the IFS instrument (Greco & Brandt 2016; Delorme et al. 2017).

Figure 2 (panel e) shows the best-fit BT-SETTL and YSOs template spectra (*blue* and *green* color) with the underreddened spectrum of the companion candidate (*black points*). With extinction as a free parameter, the best-fit BT-SETTL model has $T_{\text{eff}} = 3500$ K, $\log(g) = 3.0$, $R_B = 1.13R_\odot$ and $A_V = 11.9$ mag (*solid line*; $\chi_r^2 \sim 0.4$), consistent with a young (very-low gravity), gravitationally contracting and embedded stellar mass companion surrounded by a lot of dust. By contrast, lower values of extinction (e.g. $A_V = 7.72$ mag, *dotted line*), gave significantly worse fits.

The best-fit template spectra correspond to early M-type (M1 to M3.5) YSOs from (i) the 1–3 Myr-old Lupus I cloud (Sz 72 and Sz 74; Alcalá et al. 2014); and (ii) the ~ 2 Myr-old cluster IC 348 (CXOU J034404.8+315739 and Cl* IC 348 LRL 215; Luhman et al. 2003). Interestingly, both the SpeX targets are located in the youngest part of the IC 348 cluster, where class 0/I objects have been identified (Luhman et al. 2003, 2016). In particular, they could also be class 0/I objects given their significantly lower differential extinction compared to the best-fit extinctions associated with the Lupus I and BT-SETTL spectra, suggesting $A_V \gtrsim 10$ mag for the companion.

Based on the empirical relationship between spectral type and effective temperature inferred in Luhman et al. (2003) for IC 348, spectral types M1–M3.5 would correspond to $T_{\text{eff}} = 3350\text{--}3700$ K, consistent with our best-fit BT-SETTL model effective temperature.

4.5. Mass estimate

Considering an extinction of $A_V = 11.9 \pm 1.0$ mag (Sec. 4.4), our de-reddened J - and H -band absolute magnitudes are 5.3 ± 0.3 mag and 4.2 ± 0.1 mag (using Cardelli et al. 1989), respectively. We compared the absolute magnitudes and colors with BCAH98, AMES-Cond and BT-SETTL (Chabrier et al. 2000; Baraffe et al. 1998; Allard et al. 2003) models that suggests a mass of $\sim 0.10\text{--}0.25 M_\odot$. Comparing the T_{eff} and age with stellar isochrones (Baraffe et al. 2015) suggest a mass of $0.25\text{--}0.5 M_\odot$ (Table 2). Considering that this estimate assumes an age of 1 Myr — the youngest available, but an upper limit for MWC 297 (Vioque et al. 2018 suggest $\approx 0.02\text{--}0.03$ Myr) — the companion mass

may be lower. This is consistent with the best fit YSOs and SpeX template spectra with mass $\sim 0.45\text{--}0.50 M_\odot$, targets older (1–3 Myr) than MWC 297. For the 2015 epoch, we estimated the mass using only the dereddened absolute H -band magnitude, due to the lack of obvious detection in other bands.

5. DISCUSSION

The 0.8% probability of being a background star (Sec. 4.3.1) suggests that the detected point source is a bound companion to MWC 297. Our spectral analysis (Sec. 4.4) further argues in favor of a young and embedded early M-dwarf. BT-SETTL models are uncertain at low gravity (e.g. Bonnefoy et al. 2014), and the template library lacks spectra younger than 1 Myr old, both suggesting an even less massive object. Moreover, the spectral fit is not able to reproduce exactly the observed spectrum (Fig. 2, panel e). Using dust extinction curves different from those assumed for the ISM may also improve the fit (e.g. Marocco et al. 2014). Furthermore, the very red slope possibly is partially due to excess dust thermal emission from a circum-secondary disk (e.g. Christiaens et al. 2018) - with less extinction needed. Follow-up observations at longer wavelengths are required to better refine the characteristics of the companion and test the presence of a hot circum-secondary disk component.

Our detected low-mass companion might be carving the gap in dust thermal emission suggested by Alonso-Albi et al. (2009), based on the SED and 1.3 mm and 2.6 mm IRAM Plateau de Bure (PdBI) interferometer data. The resolution of the PdBI data ($1.''1 \times 0.''4$ for 1.3 mm and $1.''4 \times 0.''9$ for 2.6 mm), however, was too coarse to resolve the $0.''65$ separation between the central star and the source. Atacama Large Millimeter/submillimeter Array (ALMA) submillimeter continuum observations would allow to test whether the companion lies within a large annular gap.

Figure 3 compares our companion detection to archival data from the exoplanets.eu database assuming a companion mass of $0.25^{+0.25}_{-0.15} M_\odot$. Our target is low-mass compared to the host star and at large separation, similar to other direct imaging detections. The $\sim 10^{-2}$ mass ratio is similar to that of PDS 70 b. Interestingly, the companion around MWC 297 is one of the few discovered around young host stars (bottom panel). Most archival companions with ages below 10 Myr found with direct imaging are yet to be confirmed.

Our best-fit extinction is high, but similarly embedded young low-mass companions have been detected e.g. FW Tau C (Bowler et al. 2014) and R CrA B (Mesa et al. 2019). It may have an edge-on disk (like TWA 30 B and

Table 2. Observation log and MWC 297 B properties.

Obs. date [†]	Exp.	Track.	seeing	Δ PA	sep	sep	PA	ΔH	ΔJ	ΔY	M_B
	[s]			[deg]	[mas]	[au]	[deg]	[mag]	[mag]	[mag]	[M_\odot]
2015-04-29	1664	F	0.68	1.1	657.1 \pm 5.4	246.4 \pm 15.2	176.6 \pm 1.6	10.19 \pm 0.53	–	–	0.1–0.2
2018-07-28	5760	P	0.91	54.3	652.5 \pm 0.5	244.7 \pm 13.2	176.4 \pm 0.1	9.49 \pm 0.03	10.37 \pm 0.3	10.23 \pm 0.10	0.1–0.50

Notes. [†]Programs 095.C-0787 (PI: van den Ancker) and 0101.C-0350 (PI: Ubeira Gabellini), respectively. Table lists observation date, total integration time, telescope tracking mode (F: field-tracking; P: pupil-tracking), mean seeing, total field rotation, separation (mas and au), position angle, delta magnitude (H, J, Y) and estimated companion mass.

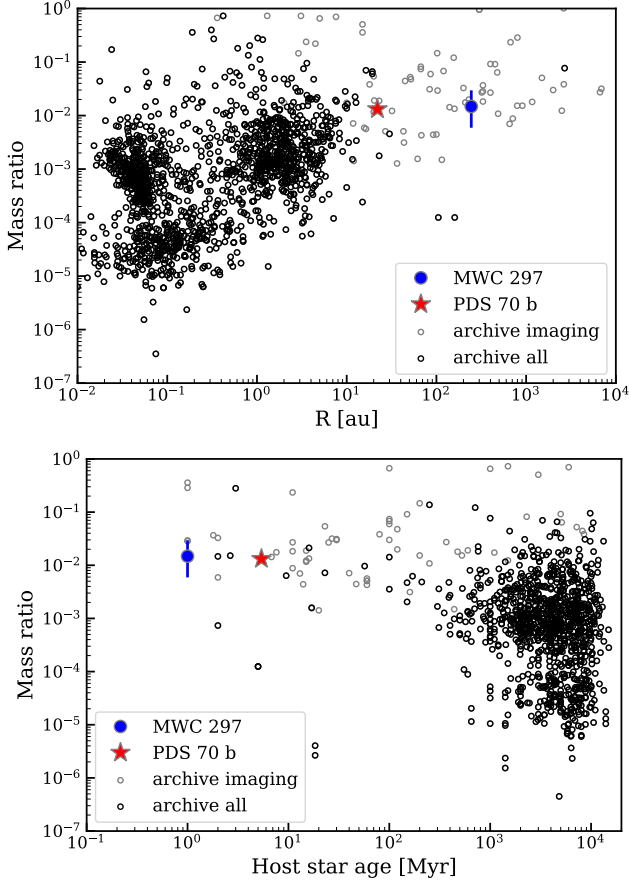


Figure 3. Ratio between companion and host stellar mass (y-axis) vs orbital separation (top) or age of stellar host (bottom). Empty circles show known exoplanets from direct imaging (gray); and other methods (black). Blue circle shows our companion MWC 297 B; red star shows PDS 70 b (Keppler et al. 2018). A companion mass of $0.25^{+0.25}_{-0.15} M_\odot$ implies a mass ratio similar to that of PDS 70 b.

FW Tau C; Looper et al. 2010; Wu & Sheehan 2017).

Follow-up with ALMA is required to confirm this for MWC 297 B.

6. SUMMARY AND CONCLUSIONS

We detected MWC 297 B in *H* band on 2015-04-29 and again in *Y*, *J* and *H* bands on 2018-07-28. Astrometry favors a gravitationally bound object. Spectral characterization suggests a young (<1 Myr) low-mass companion ($0.25^{+0.25}_{-0.15} M_\odot$) and high extinction ($A_V \sim 11.9$ mag). The large separation supports formation via gravitational instability. The mass ratio is comparable to that of PDS 70 b, but in the stellar mass regime, suggesting a similar formation process for low-mass companions around high- and low-mass stars. Finally, the companion could be responsible for the dust gap inferred by Alonso-Albi et al. (2009).

ACKNOWLEDGEMENTS

We thank the anonymous referee for providing insightful comments. We used the SPHERE Data Centre, operated by OSUG/IPAG (Grenoble), PYTHEAS/LAM/CeSAM (Marseille), OCA/Lagrange (Nice) and Observatoire de Paris/LESIA (Paris) with funding from Labex OSUG@2020 (Investissements d’avenir ANR10 LABX56). We thank P. Delorme, S. Moehler, M. Reggiani and E. Sissa for useful discussions. DF acknowledges funding from the Italian Ministry of Education, Universities and Research, project SIR (RBSI14ZRRH). GL, MGUG and CFM received funding from the European Union Marie Skłodowska-Curie grant 823823 (RISE DUSTBUSTERS project). VC and DP acknowledge Australian Research Council funding via DP180104235. CFM acknowledges an ESO fellowship.

REFERENCES

- Absil, O., Milli, J., Mawet, D., et al. 2013, *A&A*, 559, L12
 Acke, B., & van den Ancker, M. E. 2006, *A&A*, 457, 171
 Alcalá, J. M., Natta, A., Manara, C. F., et al. 2014, *A&A*, 561, A2
 Allard, F., Guillot, T., Ludwig, H.-G., et al. 2003, in *IAU Symposium*, Vol. 211, *Brown Dwarfs*, ed. E. Martín, 325
 Allard, F., Homeier, D., & Freytag, B. 2012, *Phil. Trans. Roy. Soc. A*, 370, 2765

- Alonso-Albi, T., Fuente, A., Bachiller, R., et al. 2009, *A&A*, 497, 117
- Baraffe, I., Chabrier, G., Allard, F., & Hauschildt, P. H. 1998, *A&A*, 337, 403
- Baraffe, I., Homeier, D., Allard, F., & Chabrier, G. 2015, *A&A*, 577, A42
- Beuzit, J.-L., Feldt, M., Dohlen, K., et al. 2008, in *Proc. SPIE*, Vol. 7014, Ground-based and Airborne Instrumentation for Astronomy II, 701418
- Bonnefoy, M., Chauvin, G., Lagrange, A. M., et al. 2014, *A&A*, 562, A127
- Bonnell, I., Martel, H., Bastien, P., Arcoragi, J.-P., & Benz, W. 1991, *ApJ*, 377, 553
- Bonnell, I. A. 1994, *MNRAS*, 269, 837
- Bowler, B. P. 2016, *PASP*, 128, 102001
- Bowler, B. P., Liu, M. C., Kraus, A. L., & Mann, A. W. 2014, *ApJ*, 784, 65
- Burgasser, A. J. 2014, in *Astronomical Society of India Conference Series*, Vol. 11, , 7–16
- Cardelli, J. A., Clayton, G. C., & Mathis, J. S. 1989, *ApJ*, 345, 245
- Chabrier, G., Baraffe, I., Allard, F., & Hauschildt, P. 2000, *ApJ*, 542, 464
- Christiaens, V., Casassus, S., Absil, O., et al. 2018, *A&A*, 617, A37
- . 2019, *MNRAS*, 486, 5819
- Delorme, P., Schmidt, T., Bonnefoy, M., et al. 2017, *A&A*, 608, A79
- Drew, J. E., Busfield, G., Hoare, M. G., et al. 1997, *MNRAS*, 286, 538
- Gaia Collaboration, Brown, A. G. A., Vallenari, A., et al. 2018, *A&A*, 616, A1
- Girardi, L., Groenewegen, M. A. T., Hatziminaoglou, E., & da Costa, L. 2005, *A&A*, 436, 895
- Gomez Gonzalez, C. A., Wertz, O., Absil, O., et al. 2017, *AJ*, 154, 7
- Greco, J. P., & Brandt, T. D. 2016, *ApJ*, 833, 134
- Keppler, M., Benisty, M., Müller, A., et al. 2018, *A&A*, 617, A44
- Kurucz, R. 1991, Davis Philip A.G., Upgren A.R. and Janes K.A., (eds.). L. Davis Press, Schenectady, 27
- Looper, D. L., Bochanski, J. J., Burgasser, A. J., et al. 2010, *AJ*, 140, 1486
- Luhman, K. L., Esplin, T. L., & Loutrel, N. P. 2016, *ApJ*, 827, 52
- Luhman, K. L., Stauffer, J. R., Muench, A. A., et al. 2003, *ApJ*, 593, 1093
- Macintosh, B., Graham, J. R., Ingraham, P., et al. 2014, *Proc. Nat. Acad. Sci.*, 111, 12661
- Maire, A.-L., Langlois, M., Dohlen, K., et al. 2016, *Society of Photo-Optical Instrumentation Engineers (SPIE) Conference Series*, Vol. 9908, SPHERE IRDIS and IFS astrometric strategy and calibration, 990834
- Manara, C. F., Frasca, A., Alcalá, J. M., et al. 2017, *A&A*, 605, A86
- Manara, C. F., Testi, L., Rigliaco, E., et al. 2013, *A&A*, 551, A107
- Mannings, V. 1994, *MNRAS*, 271, 587
- Manoj, P., Ho, P. T. P., Ohashi, N., et al. 2007, *ApJL*, 667, L187
- Marocco, F., Day-Jones, A. C., Lucas, P. W., et al. 2014, *MNRAS*, 439, 372
- Marois, C., Lafrenière, D., Doyon, R., Macintosh, B., & Nadeau, D. 2006, *ApJ*, 641, 556
- Marois, C., Macintosh, B., & Véran, J.-P. 2010, in *Society of Photo-Optical Instrumentation Engineers (SPIE) Conference Series*, Vol. 7736, *Proc. SPIE*, 77361J
- Meeus, G., Waters, L. B. F. M., Bouwman, J., et al. 2001, *A&A*, 365, 476
- Mesa, D., Bonnefoy, M., Gratton, R., et al. 2019, *A&A*, 624, A4
- Nelder, J. A., & Mead, R. 1965, *The Computer Journal*, 7, 308. <https://doi.org/10.1093/comjnl/7.4.308>
- Pueyo, L., Crepp, J. R., Vasisht, G., et al. 2012, *ApJS*, 199, 6
- Soummer, R., Pueyo, L., & Larkin, J. 2012, *ApJL*, 755, L28
- Sparks, W. B., & Ford, H. C. 2002, *ApJ*, 578, 543
- Tohline, J. E. 2002, *ARA&A*, 40, 349
- van den Ancker, M. E., de Winter, D., & Tjin A Djie, H. R. E. 1998, *A&A*, 330, 145
- Vioque, M., Oudmaijer, R. D., Baines, D., Mendigutía, I., & Pérez-Martínez, R. 2018, *A&A*, 620, A128
- Weigelt, G., Grinin, V. P., Groh, J. H., et al. 2011, *A&A*, 527, A103
- Wertz, O., Absil, O., Gómez González, C. A., et al. 2017, *A&A*, 598, A83
- Wu, Y.-L., & Sheehan, P. D. 2017, *ApJL*, 846, L26